CFD Simulation of an Inward-Turning Supersonic Inlet Unstart at Flight Mach Number 1.7

Charles J. Trefny[1]
NASA Glenn Research Center, Cleveland, Ohio, 44135

Abstract

Interest in inward-turning inlets for low supersonic Mach number applications emerged during NASA's Commercial Supersonic Technology Project, as a means of reducing disturbances caused by propulsion integration. Inward-turning designs have the potential to greatly reduce the strength of shock waves emanating outward from the nacelle, and therefore their contribution to the overall sonic boom signature. For top-mounted, or over-wing installations, disturbances to aircraft aerodynamics are reduced. The nature of the inward-turning geometry results in a boundary-layer thickening effect, opposite that of the familiar thinning of an outward-turning cone boundary-layer. The application of a small amount of boundary-layer bleed at the throat has been shown to alleviate the negative effects of the boundary-layer on subsonic diffuser performance. Boundary-layer bleed, however, comes at the expense of increased complexity, and external disturbances at bleed exits that would partially defeat the purpose of the inward-turning scheme. Vortex generators were proposed as an alternative to bleed, and an initial CFD study of their effectiveness in this application forms the basis of the present work. A source-term model in the Wind-US CFD code was used to model the effects of an array of vortex generators placed at the entrance to the subsonic diffuser. Baseline results with no vortex generators compared favorably to previously reported results with no bleed at back-pressures near the design point, but stability margin in the present case was limited by a curious non-linear phenomena similar to unstart in mixed-compression inlets. While some improvement was noted with vortex generators, their effectiveness was diminished by the limited stability margin. A time-accurate calculation was subsequently performed to better understand this process. Results of this calculation are presented and instantaneous solutions are compared with steady-state, subcritical results previously reported. The stability margin limitation is attributed to the use of a constant-pressure outflow boundary condition, which differed from that used in the prior simulations.

---

[1] Aerospace Engineer, Inlets and Nozzles Branch, 21000 Brookpark Rd. Mail Stop 5-11, NASA Glenn Research Center, AIAA Senior Member

I. Nomenclature

M = Mach number
m = Mass flow
P = Pressure
T = Temperature
x = Axial distance from focal point of parent flowfield

<u>Subscripts</u>
0 = Freestream
2 = Aerodynamic Interface Plane (AIP)
b = Back-pressure boundary condition imposed at cold-pipe outflow
T = Stagnation condition
x = Conditions on exit ray of Busemann flowfield downstream of shock

II. Introduction

Interest in inward-turning inlets for low supersonic Mach number applications emerged during NASA's Commercial Supersonic Technology Project, as a means of reducing disturbances caused by propulsion integration. Inward-turning designs have the potential to greatly reduce the strength of shock waves emanating outward from the nacelle, and therefore their contribution to the overall sonic boom signature. For top-mounted, or over-wing installations, disturbances to aircraft aerodynamics are reduced. An important premise is that the streamline-tracing technique will result in an internal compression geometry with the subcritical spillage characteristics of an external-compression inlet. To fully exploit this concept, a finite internal cowl lip angle must necessarily be designed into the compression surface. In Ref. [1], Otto, et al. presented a solution to merging the flowfield resulting from the leading internal conical shock wave with that of an inward-turning Busemann isentropic compression. This technique, along with a strong oblique shock wave formed the basis of the inlet architecture presented and analyzed in that article. The nature of the inward-turning geometry results in a boundary-layer thickening effect, opposite that of the familiar thinning of an outward-turning cone boundary-layer. Also, the boundary-layer thickness at the throat plane varies around the periphery, being thickest at the longest traced streamline. These factors result in unfavorable subsonic diffuser performance. The application of a small amount of boundary-layer bleed at the throat was investigated in Ref. [1] and found to improve both total pressure recovery and distortion to acceptable levels. While boundary-layer bleed was effective, it comes at the expense of increased complexity, and likely external disturbance at bleed exits that would partially defeat the purpose of the inward-turning scheme. As a follow-on to the Ref. [1] work, it was proposed that vortex generators be studied as an alternative to boundary-layer bleed. That study is the subject of this report.

The Mach 1.7 inlet design will be described briefly, followed by a discussion of the numerical methods used. Results with no vortex generators are presented first, where an unexpected unstart phenomena was revealed before the expected maximum back-pressure was reached. These results are compared to the no-bleed cases presented in Ref. [1]. Next, results with a co-rotating array of vortex generators are presented, with a similar back-pressure limitation. The effect of vortex generators is then compared to that of boundary-layer bleed. Finally, a time-accurate CFD analysis was undertaken to better understand the unstart phenomena that limited the sub-critical stability margin in the present work. These results are discussed and compared to the steady-state subcritical solutions of Ref. [1].

III. Inlet Design

The inlet architecture and sizing are the same as that shown in Ref. [1] and are repeated here for convenience. The supersonic compression surface is generated by tracing streamlines upstream in a "parent" flowfield. The parent flowfield used in this case is an axisymmetric, isentropic flow commonly referred to as a "Busemann" compression. The Busemann flow is also "conical" where flow properties are constant along rays emanating from a focal point on the axis. The basic inviscid architecture is as shown in Fig. 1, with the Mach 1.7 leading conical shock followed by the streamline-traced conical compression that terminates with a strong oblique shock. An isometric view of the flow surface from the cowl lip to the inlet throat appears in Fig. 2. Note the sharp notch at the focal point. This is a result of streamlines being traced forward from the circular inlet throat that rests on the rotational axis of the conical parent flowfield.

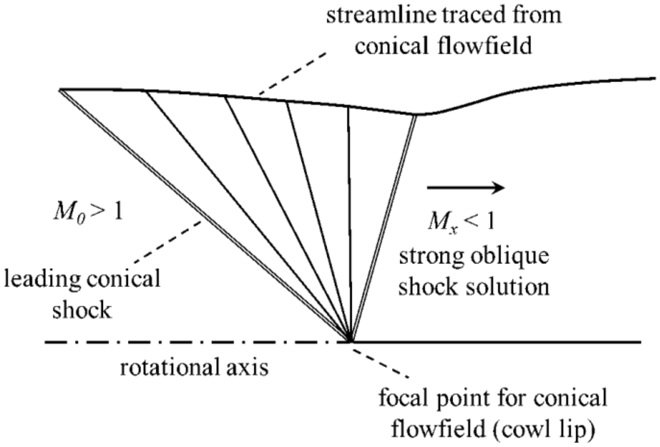

Fig. 1 Basic inviscid inlet architecture.

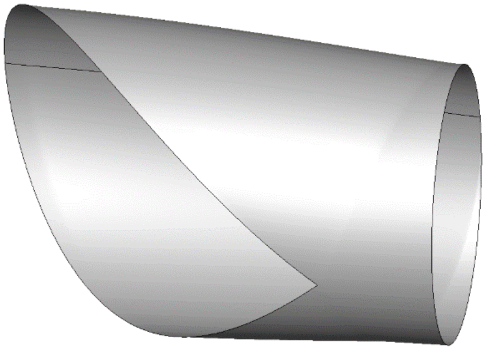

Fig. 2 Isometric view of unmodified geometry.

Modifications to this native flow surface were necessary and are as follows. The corner at the impingement line of the strong oblique or “terminal” shock wave was rounded. Then, the inlet surfaces upstream of the terminal shock were displaced radially-outward to accommodate boundary-layer growth. Finally, the sharp notch at the focal point was relieved with a larger cut-out to enable starting. More details on these modifications can be found in Ref. [1]. The inlet was scaled based on the General Electric F404-GE-102 low-bypass-ratio turbofan engine for a corrected airflow and fan face diameter of 146.3 lb⁄s and 27.9 in. respectively. The total pressure recovery was assumed to be 96.9% resulting in an inlet capture area of 552.3 in^2. The subsonic diffuser in the present work is slightly shorter than that of Ref. [1], and based on its area ratio of 1.409, has an equivalent conical angle of 2.33-degrees. An isometric view of the final inlet configuration with an external nacelle surface added is shown in Fig. 3, with the axial stations of important features noted.

A. Vortex Generators

The effect of vortex generators was assessed using a source-term model in the Wind-US code to be described later. This approach applies the local effect of individual user-defined vortex generators and eliminates the need for gridding individual vanes. An array of 24 vanes was placed 1.318-inches downstream of the throat, in a symmetric arrangement from -104 to 104-degrees about the symmetry plane. It was assumed that vortex generators would be of little to no benefit outside of this periphery due to the thin boundary-layer and absence of flow surface in the cut-out region. The individual vanes were ½-inch high, which was approximately the boundary-layer height on the symmetry plane, where it was at its maximum. No attempt was made to vary the vane height with respect to the variable thickness of the boundary layer at the throat. The vanes were given a typical[3,4] chord-to-height ratio of 2 (1-inch chord length) and a height-to-spacing ratio of 0.27 (1.85-inch spacing).

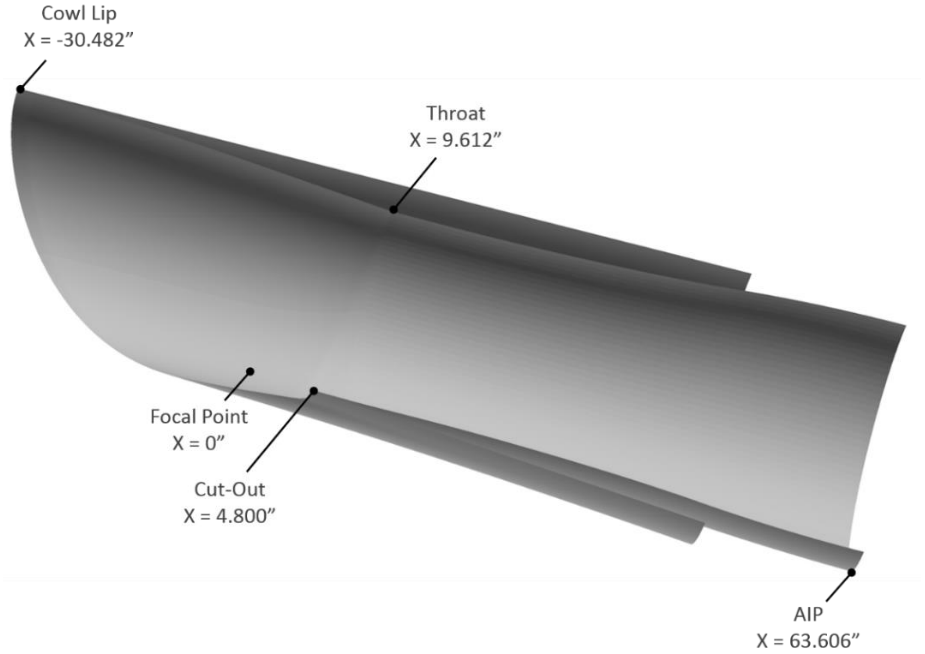

Fig. 3 Final inlet geometry.

Three different vortex generator angle-of-attack variations were screened in initial calculations at a back-pressure near the inlet design point. The first was counter-rotating pairs where, from the symmetry plane, the vane angles alternated in a +16-degree / -16-degree pattern along the starboard side, resulting in a counter-clockwise / clockwise pattern of vortices looking upstream. The next orientation was a co-rotating array with +16-degree vanes, resulting in counter-clockwise rotation. The last configuration was a -16-degree co-rotating array giving clockwise rotation. This scheme clearly provided the best flow uniformity at the AIP and was used for the balance of the present work. Fig. 4 depicts the geometry of the vortex generator array used as input to the source-term model.

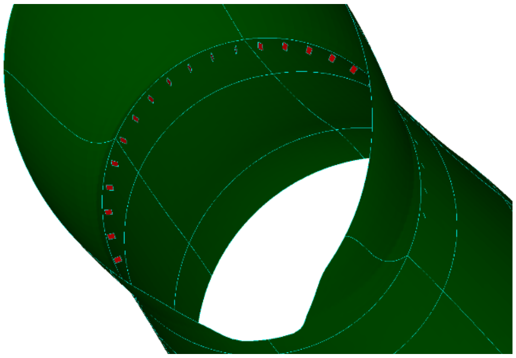

Fig. 4 Vortex generator array.

IV. Computational Method

Simulations were done using the Wind-US CFD code[2]. The flow domain was as pictured in Fig. 5, consisting of 24 blocks. Of these, 16 were internal to the inlet, 5 were external flow, and 3 comprised the cylindrical "cold-pipe" downstream of the AIP. The cold-pipe was 2.362 AIP diameters long and intended to provide a buffer between it and the constant-pressure outflow boundary condition. Table 1 lists the distribution of cells within these blocks.

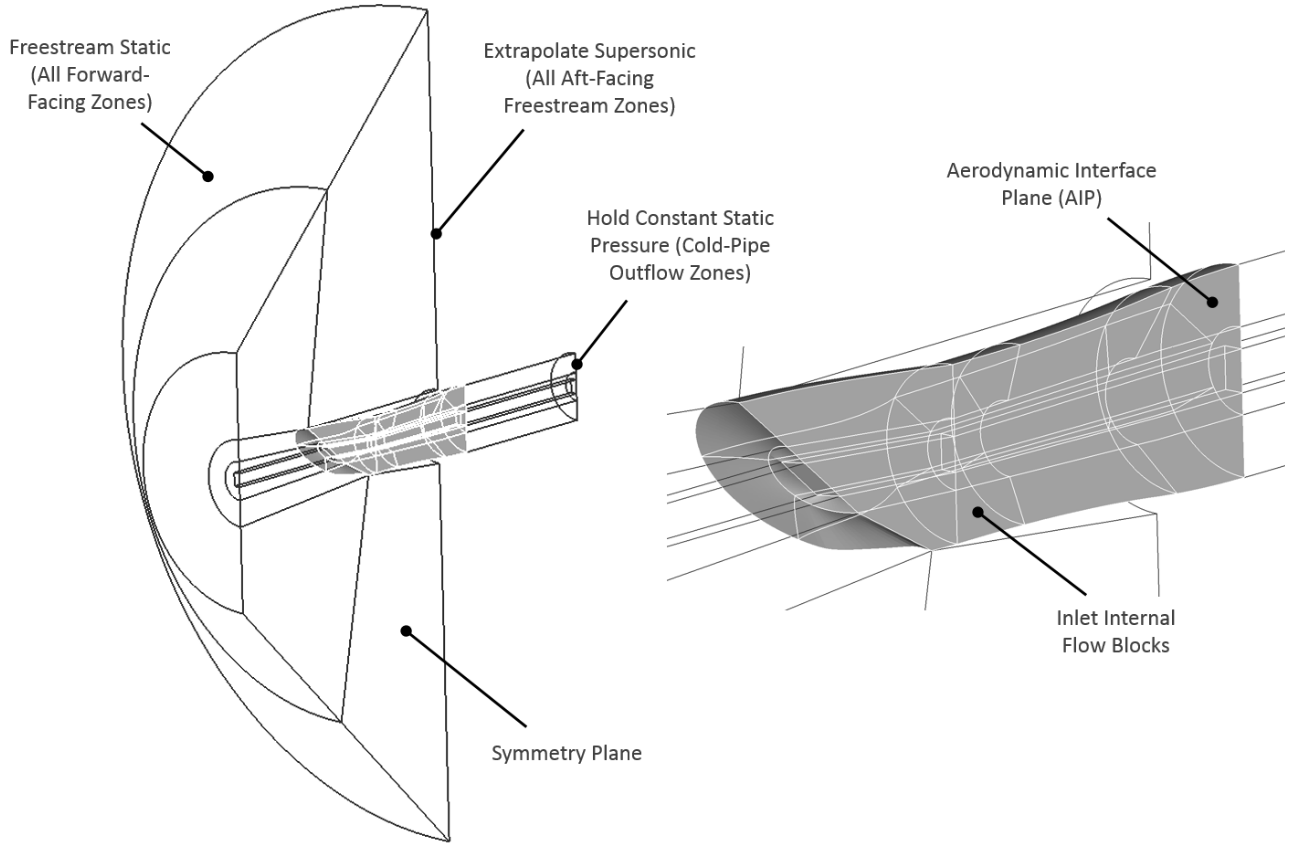

Fig. 5 Grid topology and boundary conditions.

Table 1 Grid cell distribution by block.

Internal				External		Cold-Pipe	
Block	#Cells	Block	#Cells	Block	#Cells	Block	#Cells
5	89,600	17	384,000	1	26,880	9	36,736
6	192,000	18	384,000	2	57,600	10	78,720
7	53,760	19	384,000	3	288,000	11	393,600
12	115,200	20	384,000	4	216,000	Σ:	509,056
13	320,000	21	384,000	8	216,000		
14	320,000	22	384,000	Σ:	804,480		
15	320,000	23	384,000				
16	384,000	24	384,000				
		Σ:	4,866,560			Total Cells:	**6,180,096**

Wind-US solved the Reynolds-Averaged Navier-Stokes (RANS) equations using a calorically-perfect air thermodynamic model, and the 2-eqn Menter shear stress transport (SST) turbulence model. Spatial accuracy was formally second order using the Roe flux-difference splitting upwind formulation. Freestream inflow conditions of

Mach 1.7 at an altitude of 56500 feet were imposed on forward-facing block surfaces. This corresponds to a static pressure, P_0, of 1.2306 psia, a static temperature, T_0, of 389.97 deg R, and a unit Reynolds number of 1.47 million. Supersonic extrapolation was used on freestream outflow boundaries and a constant static pressure was imposed at the cold-pipe outflow to set the desired back-pressure.

All cases were initiated using a converged solution at the previous, lower back-pressure. Calculations proceeded in time-marching mode until converged, or it was apparent that it would not converge to a steady-state solution. Mass flow at the AIP was monitored and a solution was considered converged when the fluctuation was less 0.01%. A grid convergence test was done on an initial solution using the grid sequencing function in Wind-US. It was determined that the un-sequenced grid used herein yielded grid-independent results. Grid spacing at all viscous walls upstream of the AIP was sufficiently small to maintain y+ values at 0.5 or less. For unsteady analysis of the unstart process, Wind-US was run in time-accurate mode with a time step of 4×10^{-8} seconds.

The effect of vortex generators was simulated using the BAY[3,4] model in Wind-US. This model uses source terms to generate vorticity commensurate with user-specified parameters. Transverse velocity vectors at a plane just downstream of the vortex generator array appear in Fig. 6 where the imposed counter-clockwise rotation is clearly seen.

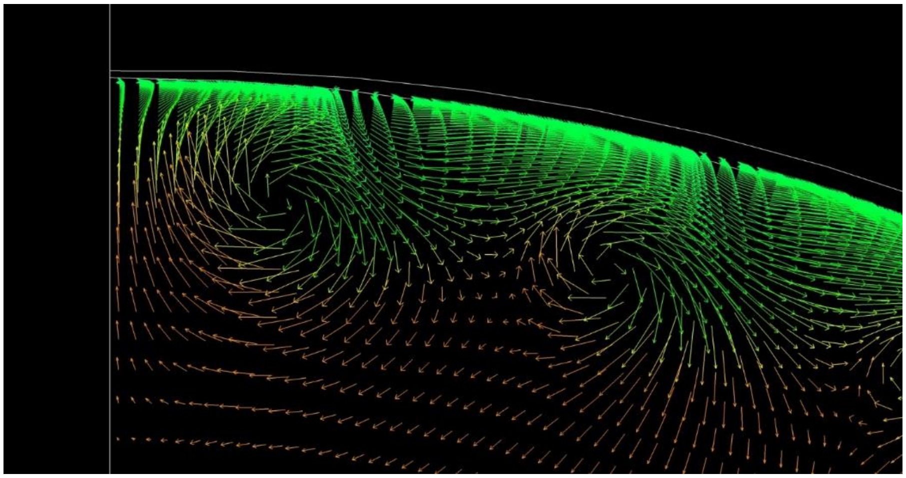

Fig. 6 Crossflow velocity, looking upstream, imposed by the BAY vortex generator model. Vectors are colored by stagnation pressure.

V. Results and Discussion

Following Ref. [1], inlet total pressure recovery and distortion were post-processed by interpolating the solution at the AIP onto a 40-probe, area-weighted rake. Total pressure recovery is simply the average of these 40 values divided by the freestream total pressure. Radial and circumferential total pressure distortion was evaluated using the General Electric “phase 0 method D” procedure of Ref. [5] on the same 40 values.

A. Results with No Vortex Generators, and Comparison to No-Bleed Cases of Ref. [1]

Calculations with no vortex generators were done first to provide baseline recovery and distortion levels for the present geometry, and to compare with the no-bleed results of Ref. [1]. Fig. 7 presents total pressure recovery and distortion over a range of back-pressure ratios compared to that of Ref. [1]. Peak recovery is roughly one-percent lower, and distortion markedly higher, remaining outside of the F404-GE-102 engine envelope[6]. This is attributed to the shorter subsonic diffuser in the present case. A striking feature in the recovery plot is the limited subcritical range of the present simulation as compared to that of Ref. [1]. A back-pressure ratio one-percent greater than the 3.893 maximum shown, resulted in an unsteady phenomena similar to unstart in a mixed-compression inlet. Further, this solution did not converge to steady-state. The increase in radial distortion for the 3.893 back-pressure case is caused by a flow feature at the AIP related to the cut-out in the cowl lip at 180-degrees.

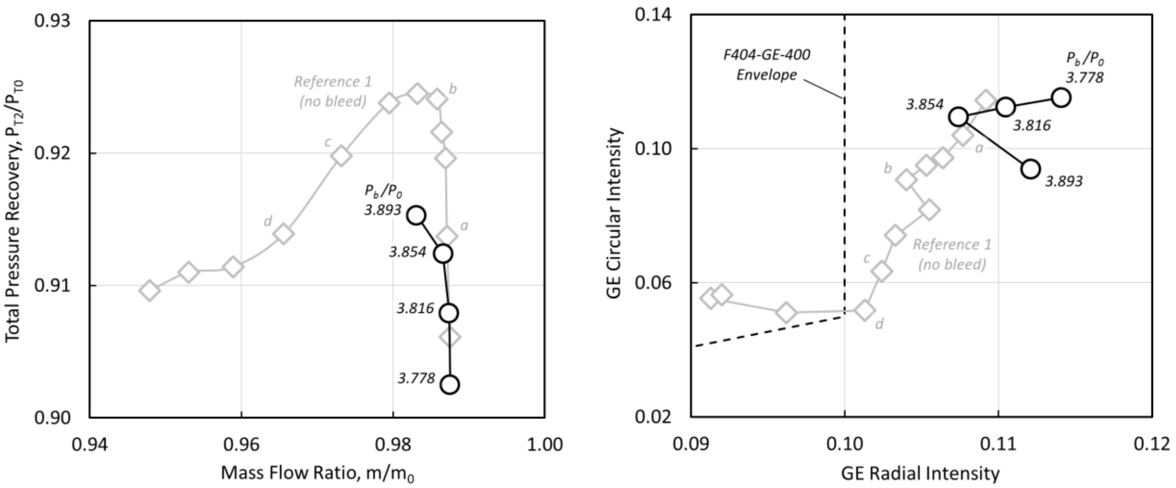

Fig. 7 Pressure recovery and distortion of cases with no vortex generators compared to that of the no-bleed cases of Ref. [1] (grey).

Mach number contours on the symmetry plane and contours of total pressure recovery at the AIP appear in Fig. 8. These provide insight into flow features and provide more comparison to the no-bleed solutions of Ref. [1]. Fig. 8a is supercritical and compares well to case ‘a’ from Ref. [1] (Fig. 8b), especially in the Taylor-Maccoll compression field and terminal shock regions. The dotted line depicts the position of the terminal shock in the parent flowfield. In general, the shock recedes from the design position due to pressure relief from flow spillage at the cut-out. Figs. 8c and 8d show the terminal shock approaching its design position as back-pressure is increased. Fig. 8d at a back-pressure ratio of 3.854 compares well with case ‘b’ from Ref. [1] in Fig. 8e. Fig. 8f depicts the highest back-pressure at which a stable solution was obtained. In this case, the aforementioned feature affecting radial distortion can be seen in the AIP total pressure ratio contours. A one-percent increase in back-pressure resulted in the flowfield of Fig. 8g. This solution did not converge but displayed a cyclic behavior during which case g was captured. The solver was not run in a time-accurate fashion, so case g cannot be considered a valid solution, beyond revealing the boundary of stable operation of the inlet. Overall, comparison to the Ref. [1] analysis is adequate for the purpose of comparing the benefits of bleed versus vortex generators at the design point. This was not unexpected given the similarities in grid topology and resolution, turbulence modeling and inlet geometry upstream of the throat. However, the issue of the very limited sub-critical range of the present analysis remains.

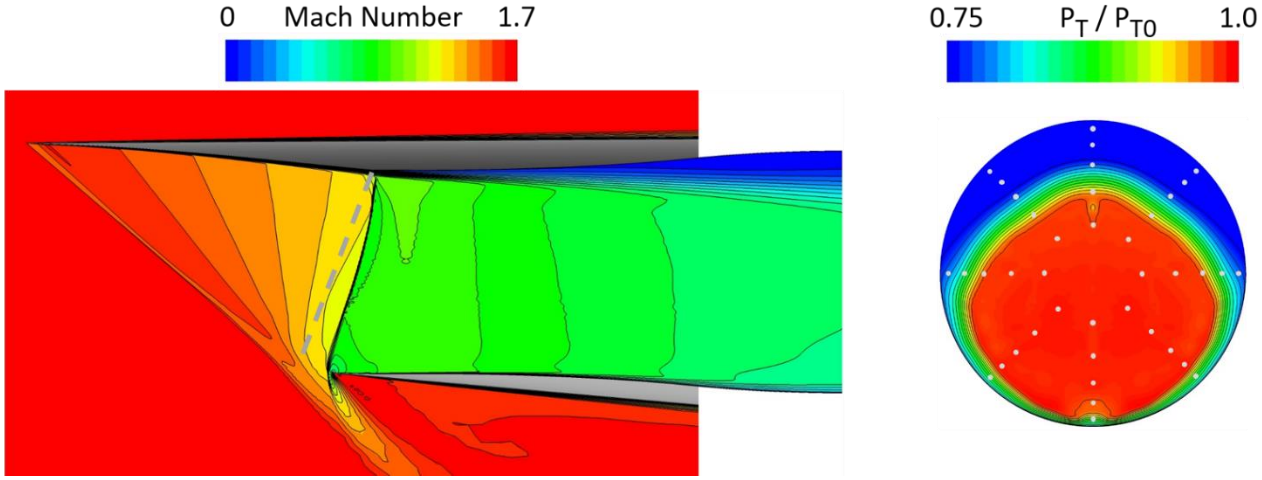

a) **$P_b / P_0 = 3.778$ (compare to no-bleed case 'a' of Ref. [1]).**

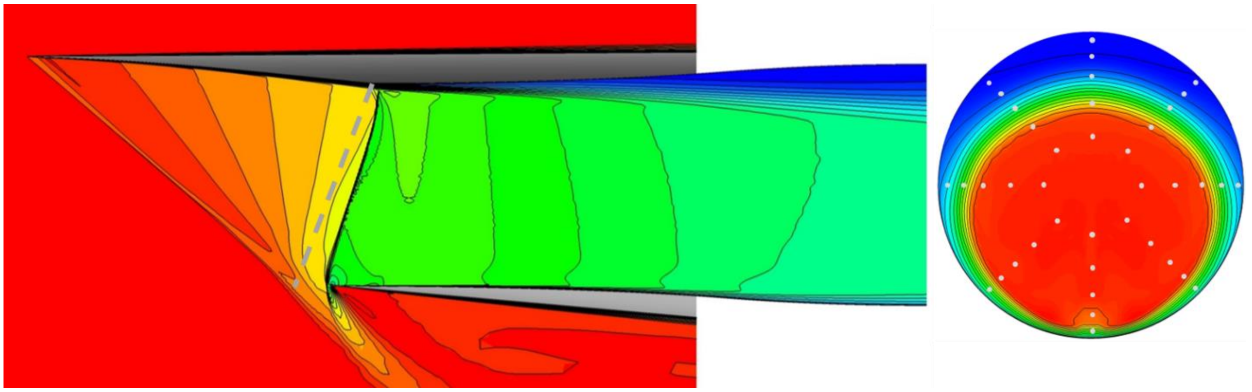

b) **No-bleed case 'a' (Ref. [1]).**

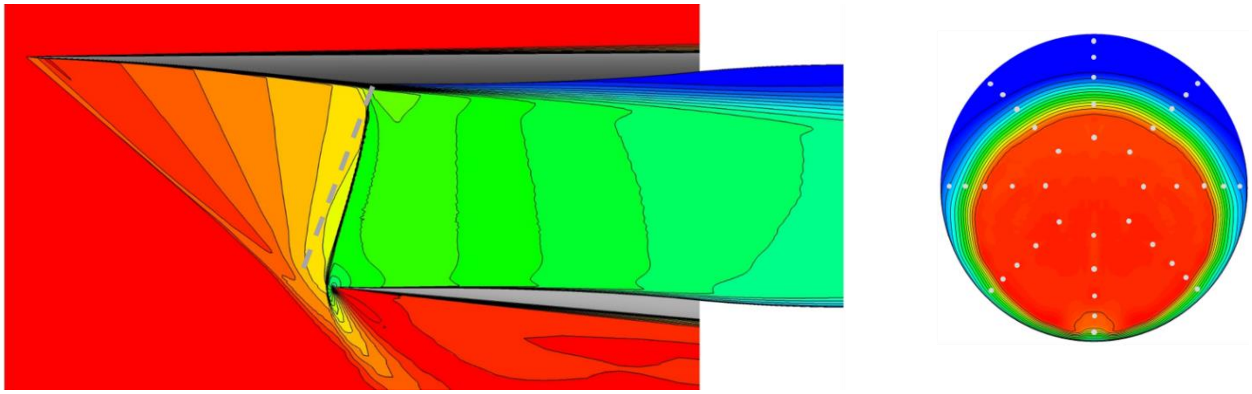

c) **$P_b / P_0 = 3.816$.**

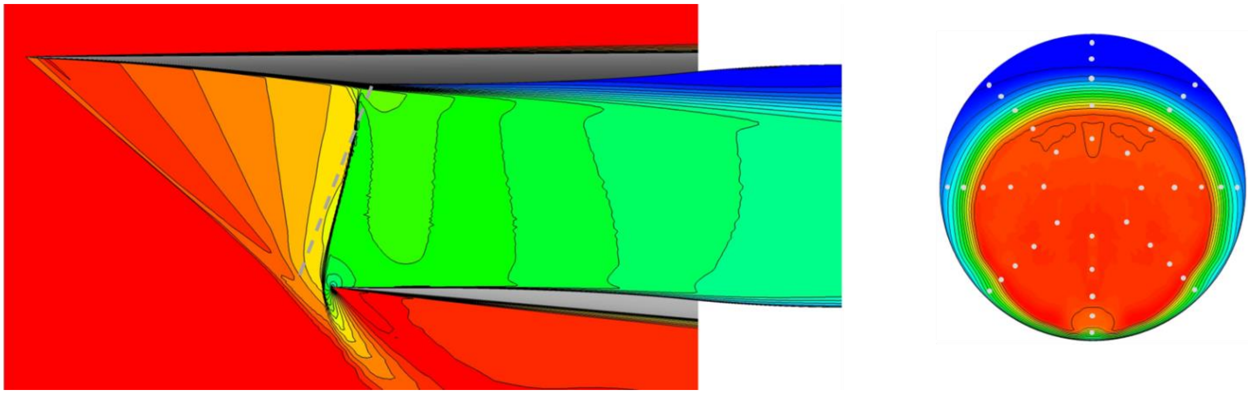

d) $P_b / P_0 = 3.854$ (compare to no-bleed case ‘b’ of Ref. [1]).

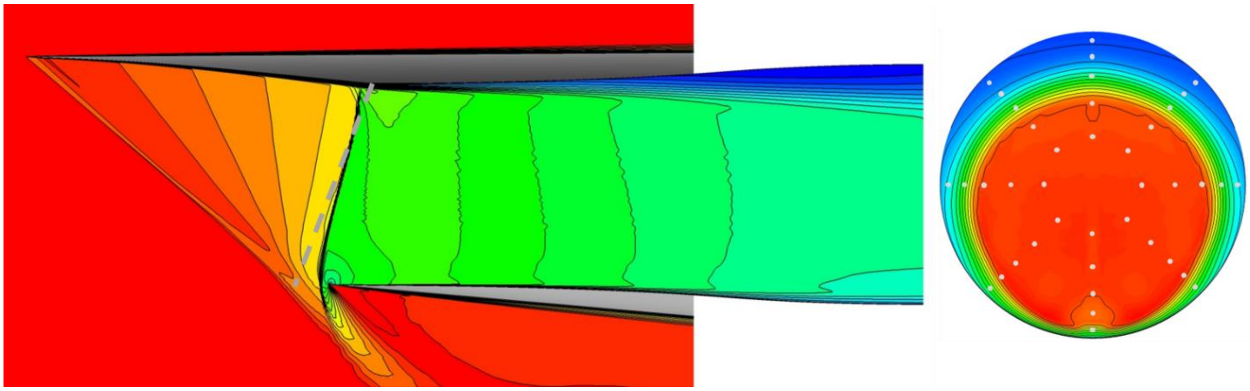

e) No-bleed case ‘b’ (Ref. [1]).

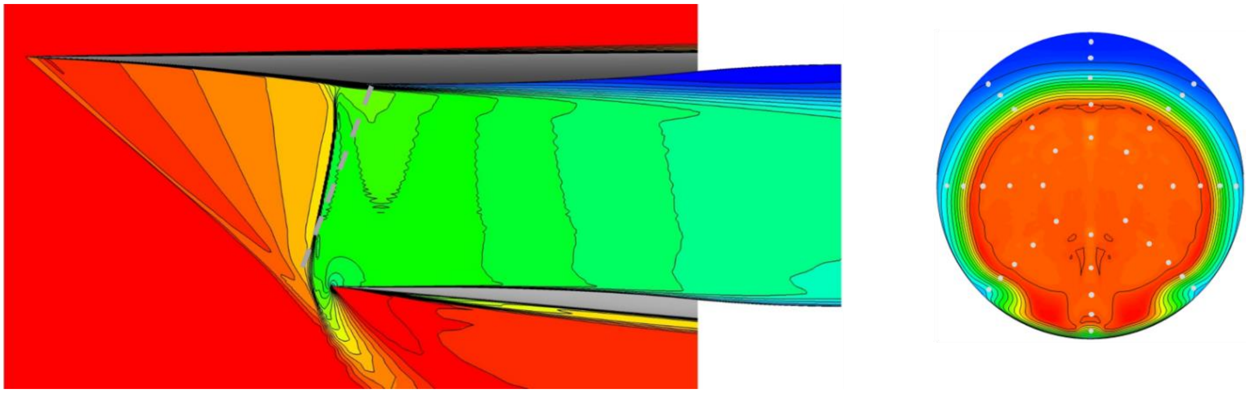

f) $P_b / P_0 = 3.893$ (max stable).

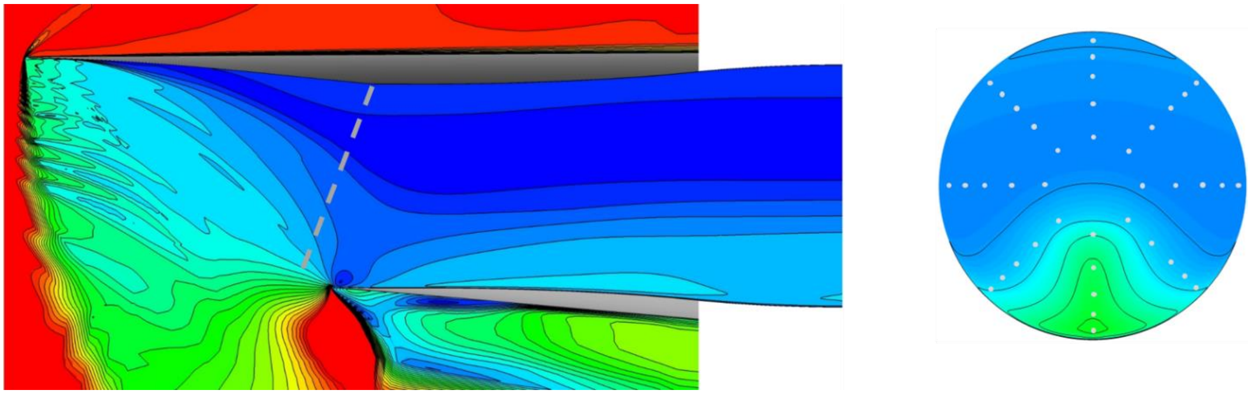

g) P_b / P_0 = 3.932.

Fig. 8 Contours of Mach number on the symmetry plane and total pressure recovery at the AIP for various back-pressure ratios with comparisons to Ref. [1].

B. Results with Vortex Generators

Inlet performance with vortex generators is compared to that with no vortex generators in Fig. 9. Since the vortex generators were proposed as an alternative to bleed, the Ref. [1] results with bleed are also shown. The subcritical range with vortex generators is even more limited than that of the baseline, and well below that of Ref. [1]. A 2% increase in the area-averaged peak recovery is noted versus the case with no vortex generators, as low-momentum flow is redistributed over the 40-probe array. The maximum recovery remains well below the Ref. [1] peak value. Distortion shows a promising trend with back pressure, and approaches the edge of the F404-GE-400 envelope, but remains outside. Note that the maximum stable back-pressure is one-half percent greater than that with no vortex generators, but this last increment was only attempted with the vortex generators present.

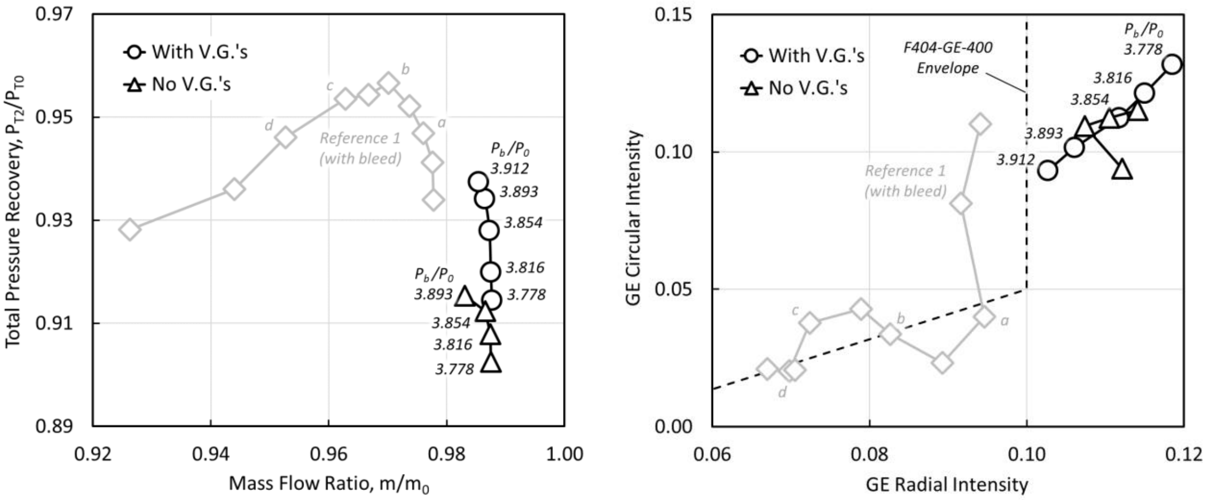

Fig. 9 Pressure recovery and distortion characteristics of cases with vortex generators compared to that of the baseline.

Similar to the baseline cases, contours of Mach number on the symmetry plane and total pressure recovery at the AIP are presented in Fig. 10 over the range of back-pressures simulated. As was the case with no vortex generators, the final increment in back-pressure resulted in unstart and the solution did not converge. While the Mach contours on the symmetry plane appear to show a significant improvement on the upper boundary of the subsonic diffuser, examination of the AIP total pressure contours reveals that much of this improvement is due to an outboard redistribution of low-momentum flow. It would appear however, that if subcritical stability margin could be increased, distortion would continue to improve with back-pressure. Optimization of the vortex generator geometry would result in further improvement. A time-accurate calculation was therefore initiated to better understand the instability, and lack of subcritical stability margin.

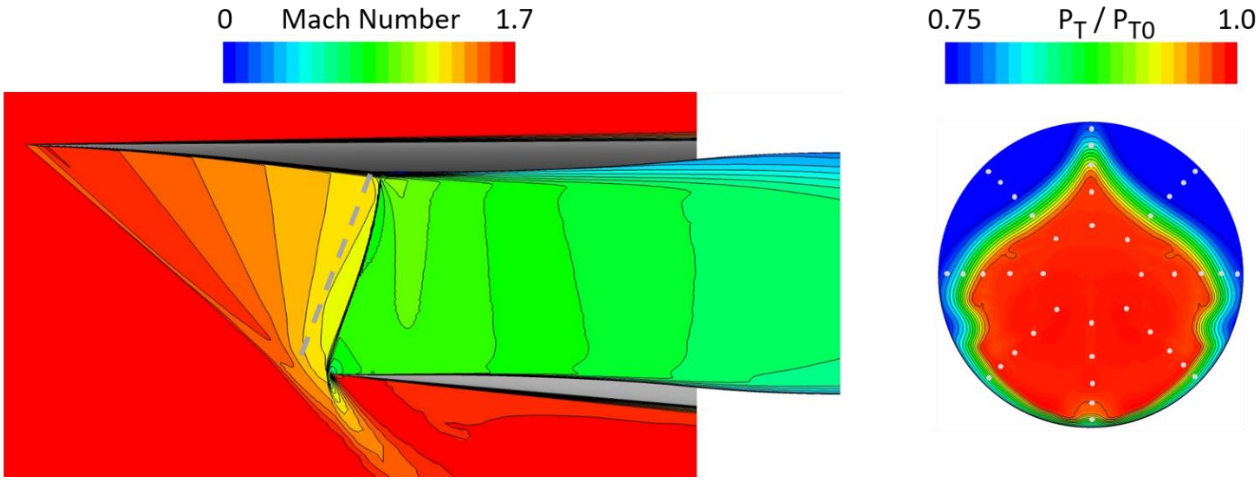

a) P_b / P_0 = 3.778.

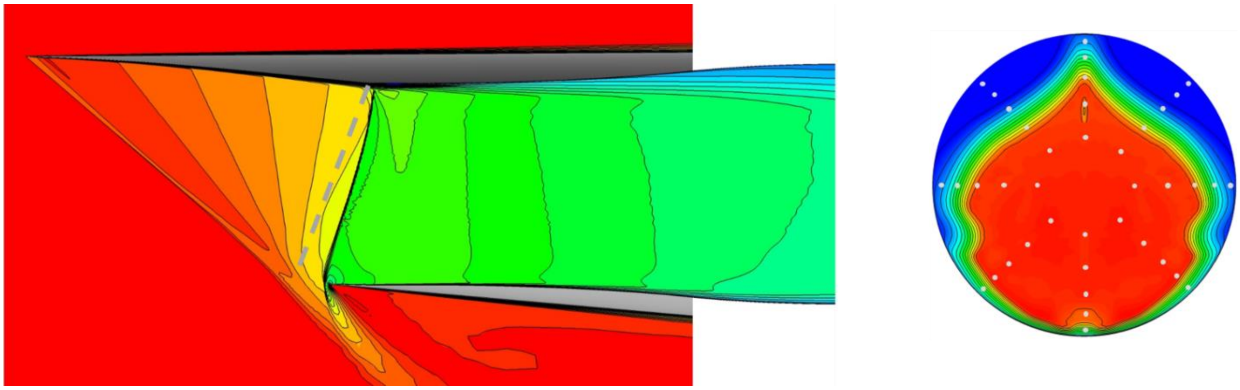

b) P_b / P_0 = 3.816.

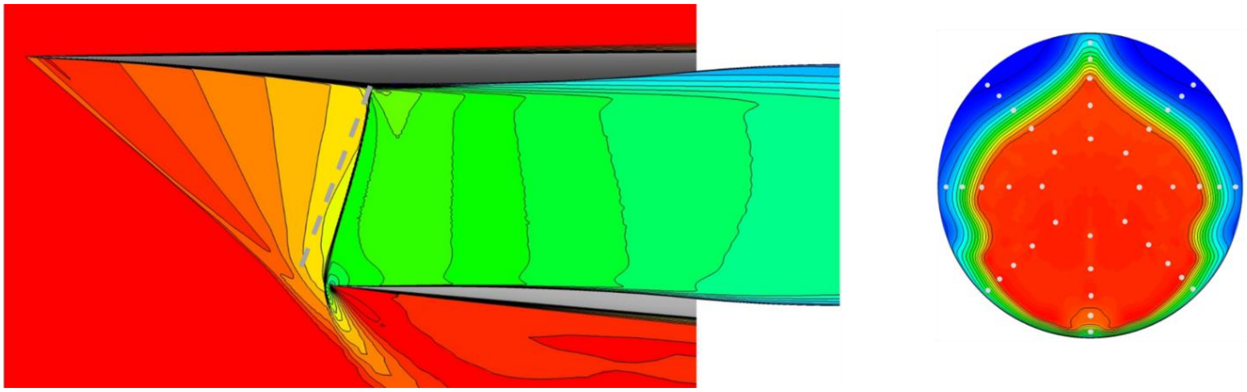

c) P_b / P_0 = 3.854.

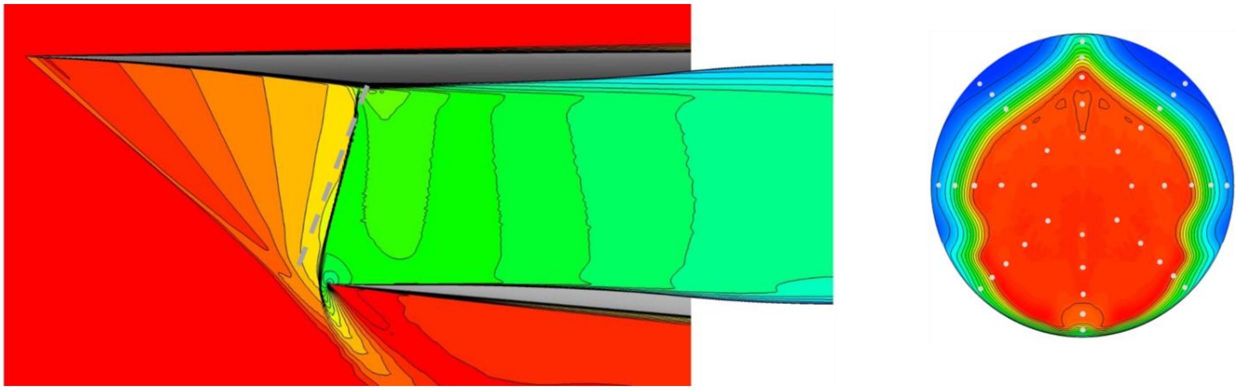

d) $P_b / P_0 = 3.893$.

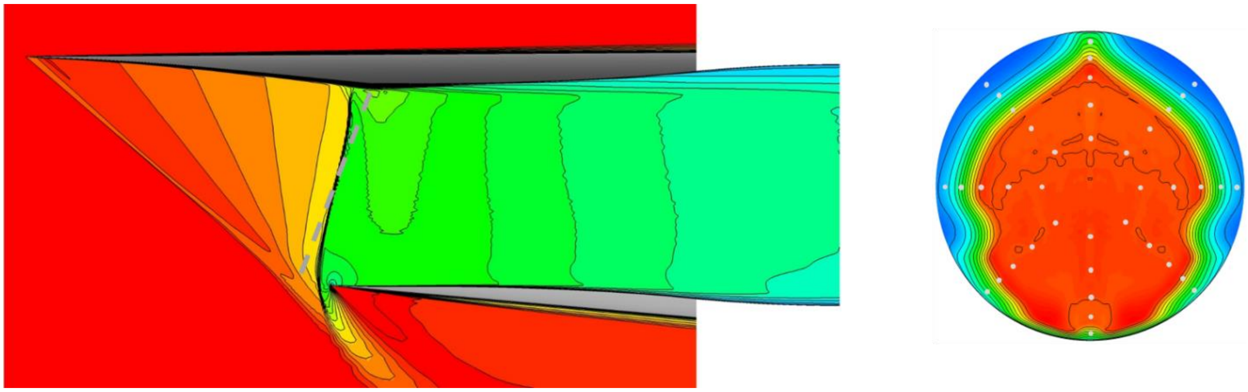

e) $P_b / P_0 = 3.912$ (max stable).

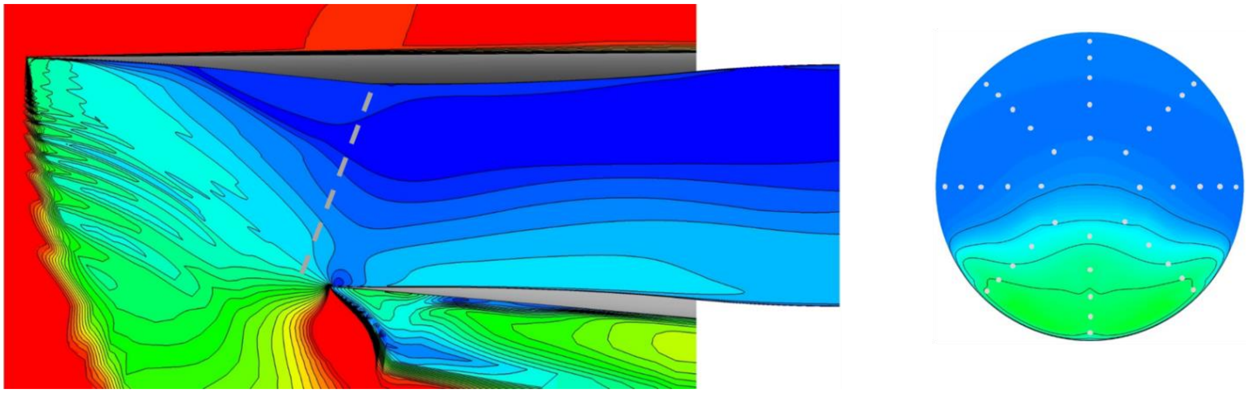

f) $P_b / P_0 = 3.932$.

Fig. 10 - Contours of Mach number on the symmetry plane and total pressure recovery at the AIP for various back-pressure ratios.

C. Time-Accurate Analysis of Unstart Phenomena

A time-accurate solution with vortex generators was initiated at a back-pressure ratio of 3.932, with the converged solution at 3.912 (Fig. 10d) as the initial condition. Fig. 11 shows instantaneous Mach contours on the symmetry plane as time advances from 0ms, to the end of the simulation at 660ms. Note the scale change in the contour plots, made to better visualize spillage in the notch region. The pressure pulse from the one-half percent increase in back-pressure arrives at the throat at 26ms. This is barely discernable in the Mach number contours, but can be seen in the static pressure distributions shown later. At 100ms (Fig. 11b), initial movement of the terminal shock can be seen. Its angle tips forward slightly in an attempt to remain aligned with a constant-pressure ray of the Taylor-Maccoll flowfield. As intended, increased spillage through the cut-out region at the lower boundary is evident. This increased spillage was intended to compensate for the reduction in airflow at the AIP, resulting in a stable flowfield. Figs. 11c-11f demonstrate that this did not happen as the shock continues to move upstream, reaching the tip of the cowl at 496ms. At this point, fluctuations in the flowfield begin to grow, with periodic behavior from approximately 610ms to the end of the simulation at 660ms. Figs. 11g and 11h show two symmetry plane Mach contours, chosen to represent approximately the minimum and maximum air capture during periodic behavior.

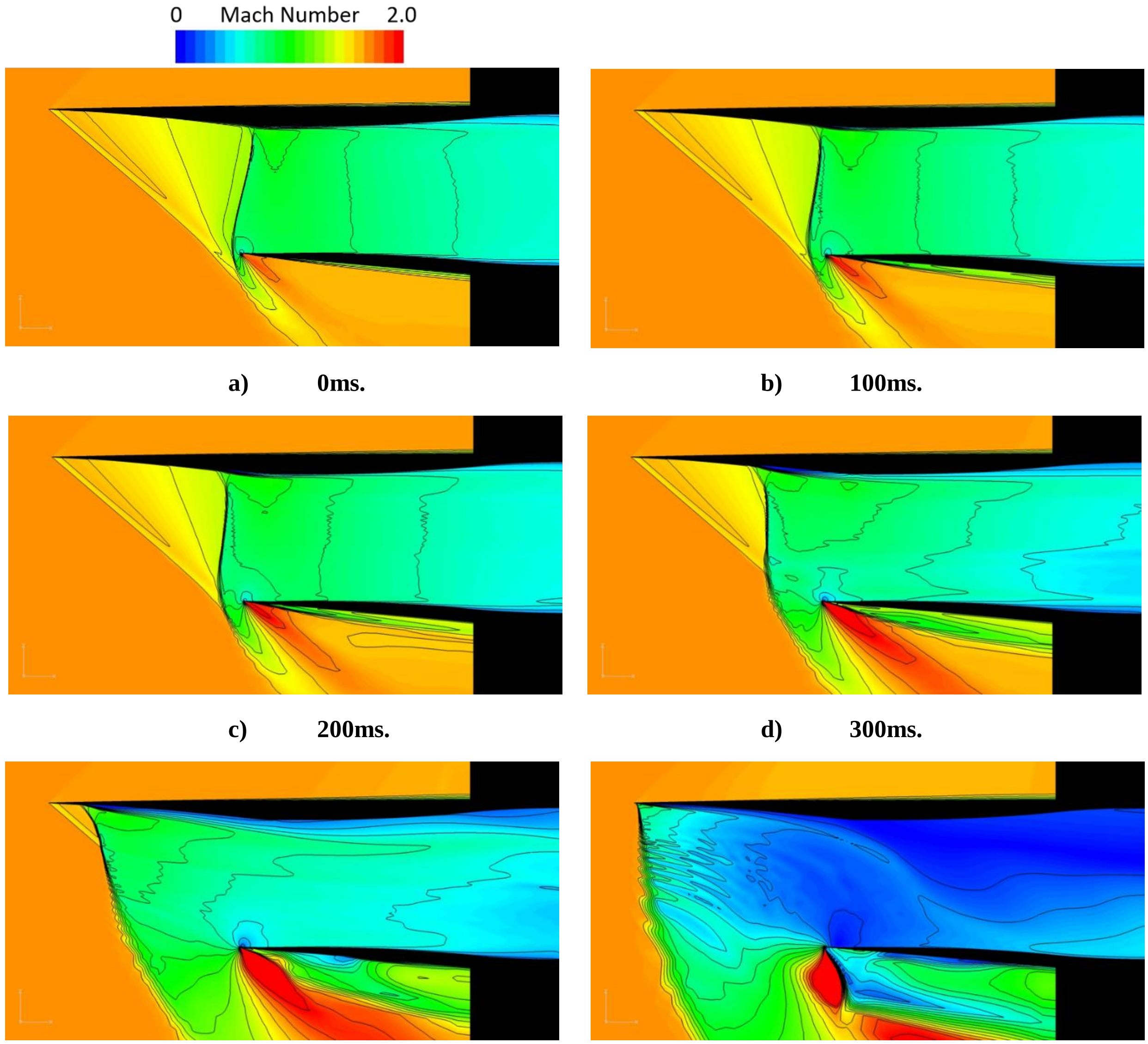

a) **0ms.**

b) **100ms.**

c) **200ms.**

d) **300ms.**

e) **400ms.**

f) **496ms.**

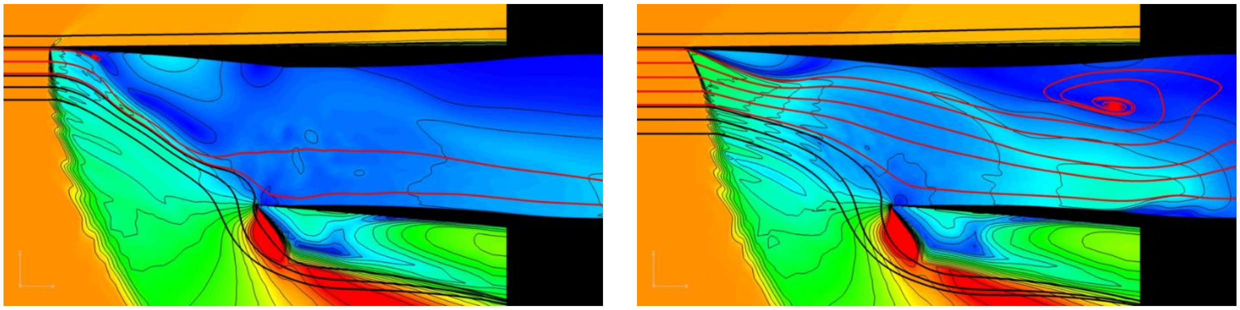

g) 618 and 644ms. h) 610, 636 and 660ms.

Fig. 11 Mach number contours on the symmetry plane at various time from back-pressure increase.

Of interest in the mechanical design of inlet structures are maximum pressure levels and frequencies of unsteady processes such as unstart and buzz. Fig. 12 presents static pressure distributions on the symmetry plane upper surface, corresponding to the time instances of Fig. 11. Note that the pressure traces end at the AIP station, and that the back-pressure is imposed at the constant-pressure outflow plane at 10.792 ft. Solid lines depict the smooth advance of the terminal shock from the inlet throat to the cowl lip at t=496ms. Dotted lines depict two points during the periodic limit-cycle behavior. Local static pressure only slightly exceeds the 3.932 back-pressure ratio imposed.

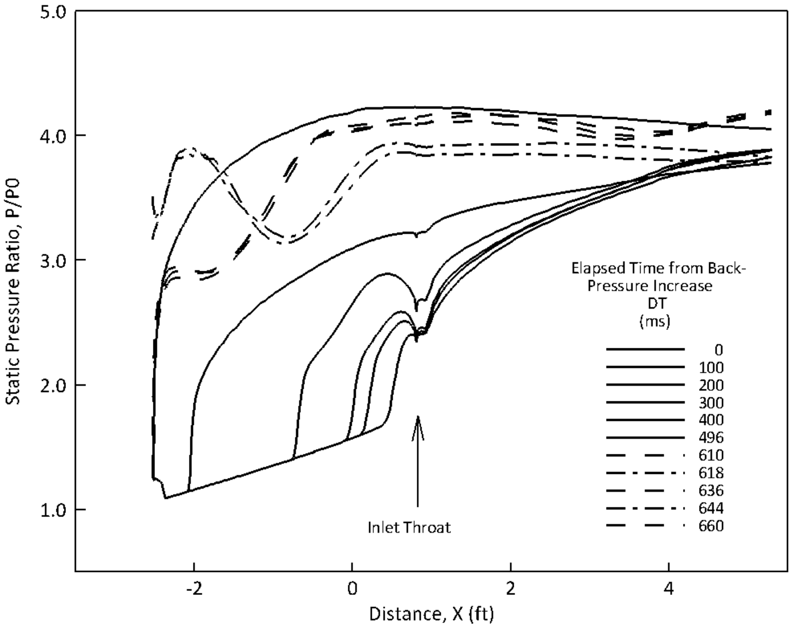

Fig. 12 Pressure distribution on symmetry plane upper surface at various elapsed times.

Fig. 13 shows the time history of static pressure at four locations on the symmetry plane during the unstart event. Fig. 13c and 13d show the slight increase in pressure at the inlet throat roughly 25ms after the step-change in back-pressure. A continuous reduction in pressure is seen at the lower cowl lip (Fig. 13b) as airflow spillage increases. Arrival of the terminal shock at the upper cowl lip is seen in Fig. 13a, followed by indication of unsteady flow, and limit cycle behavior. The flat line between spikes in Fig. 13a occurs as the terminal shock recedes back onto the compression surface. All four traces indicate the period of the limit cycle to be approximately 25ms corresponding to a frequency of 40Hz.

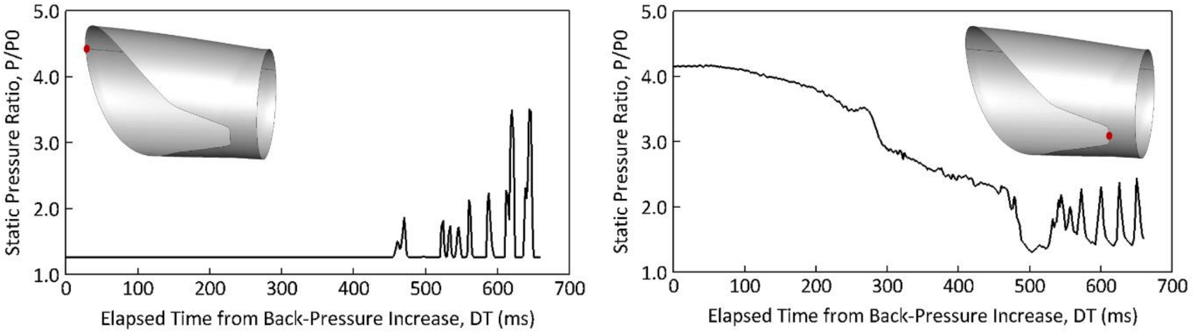

a) Upper surface cowl lip. **b) Lower surface cowl lip.**

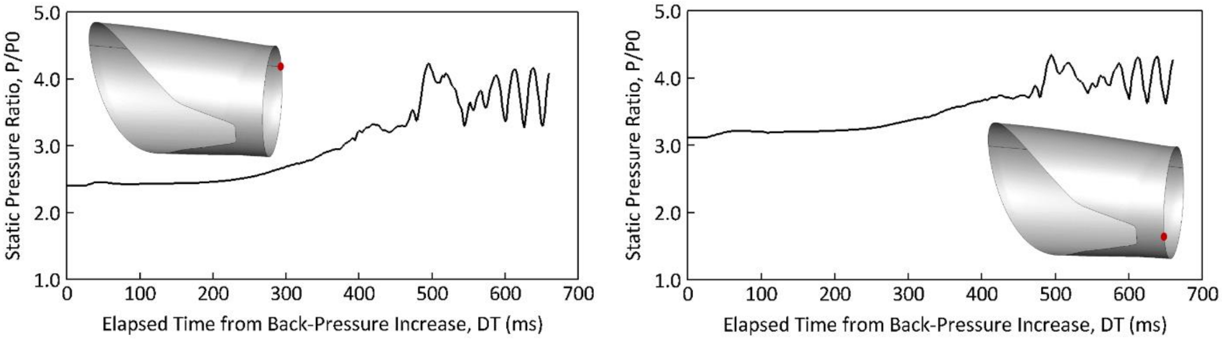

c) Upper surface throat. **d) Lower surface throat.**

Fig. 13 Pressure time histories at various points in inlet internal surface.

D. Comparison of Unsteady Solutions to Steady Subcritical No-Bleed Solutions of Ref. [1]

At specific points in time during the advance of the terminal shock, the flowfield bares striking resemblance to the ‘c’ and ‘d’ no-bleed solutions of Ref. [1]. This comparison is shown in Figs. 14 and 15. The AIP total pressure contours obviously differ due to the vortex generators in the present case, as well as the slightly shorter subsonic diffuser. Nonetheless, the total pressure levels are similar. Mach number contours on the symmetry plane, from the cowl lip through the throat region are very similar in both cases. Initially, this called into question whether or not the ‘c’ and ‘d’ solutions of Ref. [1] were truly steady. Additional analysis presented in the next section however, revealed limitations of the constant-pressure exit boundary condition that validate the subcritical Ref. [1] solutions.

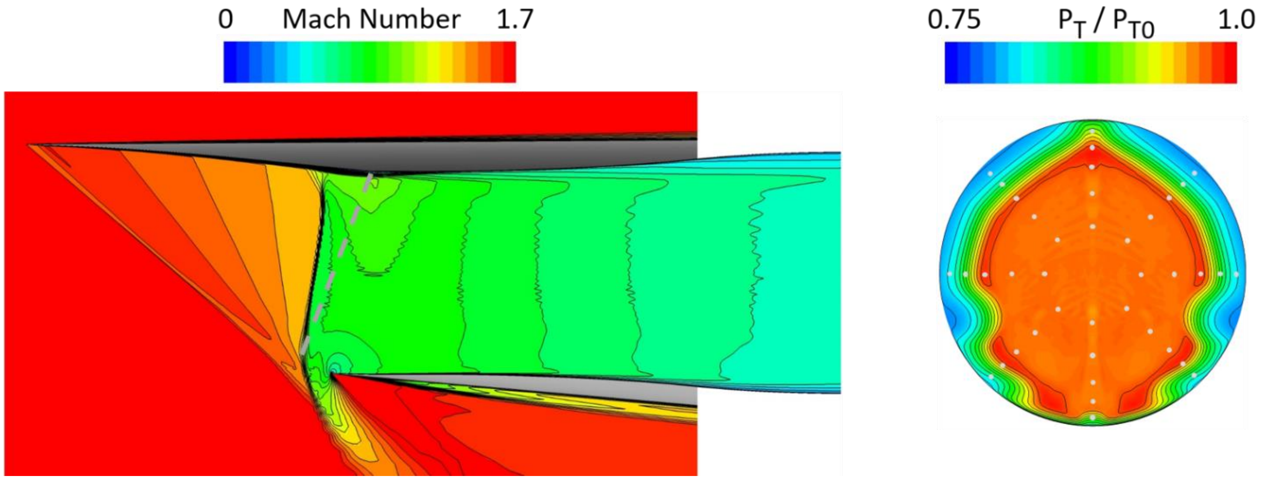

a) $P_b / P_0 = 3.932$ at 100ms from back-pressure increase.

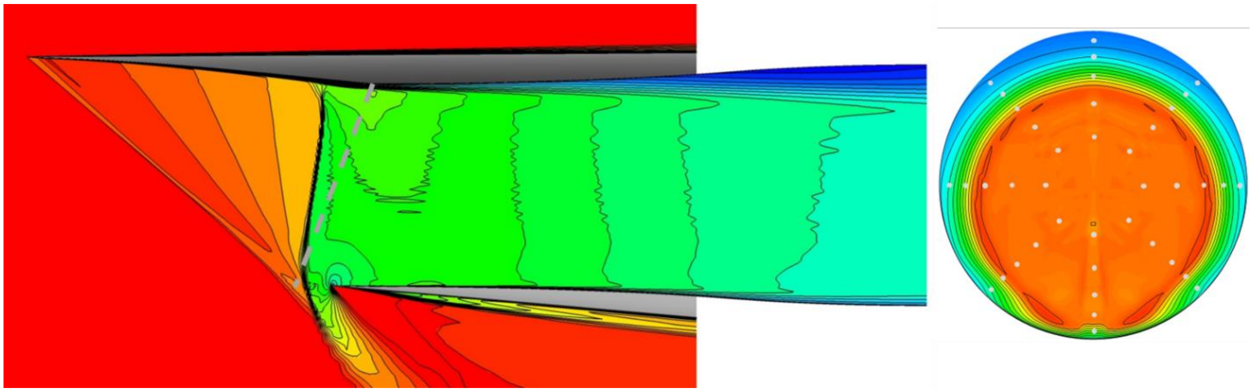

b) No-bleed case ‘c’ (Ref. [1]).

Fig. 14 Comparison of unsteady solution at 100ms to subcritical no-bleed case ‘c’ of Ref. [1]. Contours of Mach number on the symmetry plane and total pressure recovery at the AIP.

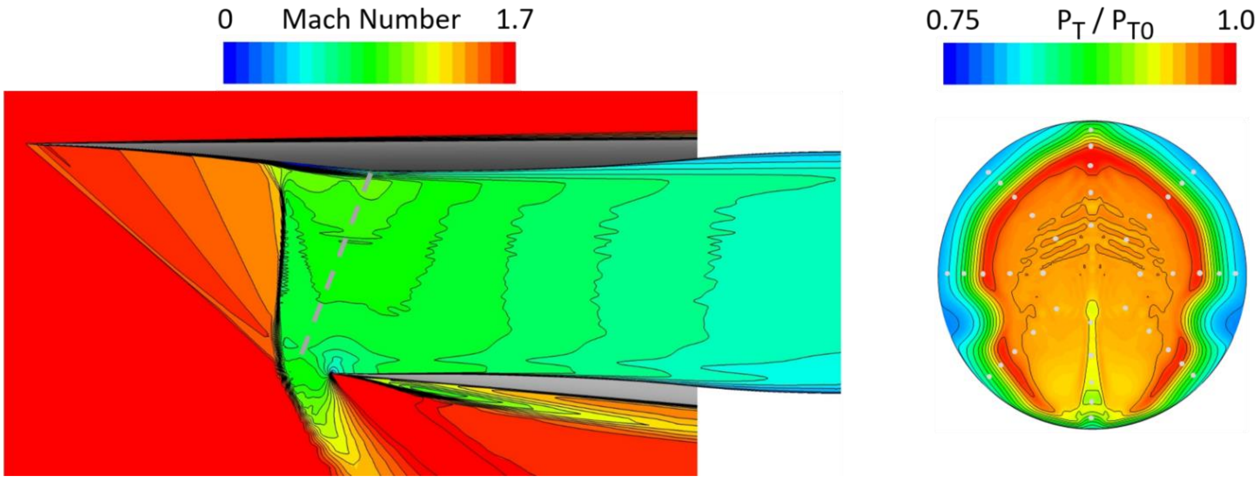

a) P_b / P_0 = 3.932 at 254ms from back-pressure increase.

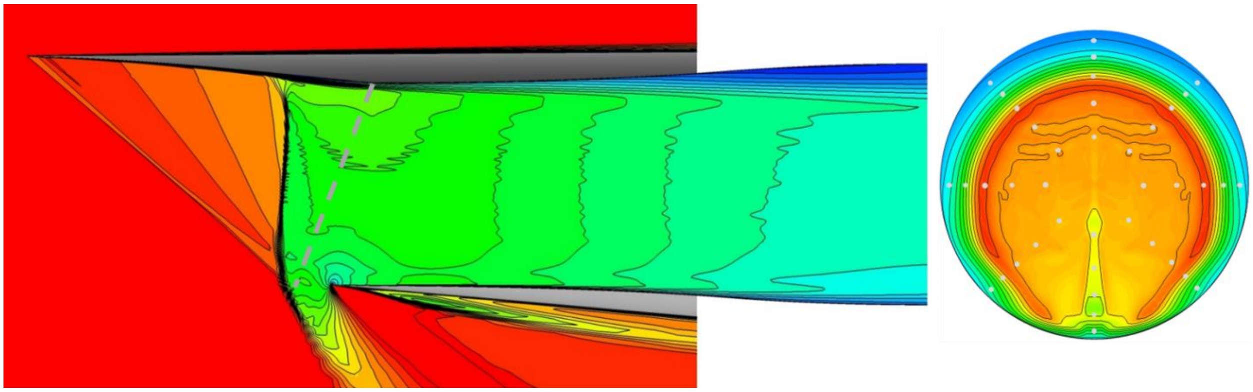

b) No-bleed case ‘d’ (Ref. [1]).

Fig. 15 Comparison of unsteady solution at 254ms to subcritical no-bleed case ‘d’ of Ref. [1]. Contours of Mach number on the symmetry plane and total pressure recovery at the AIP.

E. Limitation of Constant-Pressure Exit Boundary Condition

In hindsight, there are two factors to consider when choosing an exit boundary condition for a supersonic inlet CFD problem. First is its behavior during unstart, which will affect the dynamics of that process, and second is a physical limitation on back-pressure at sub-critical conditions. The mechanism of the unstart process in the present simulation is different than what occurs in a mixed-compression inlet, where the upstream advance of the terminal shock through a compressive flowfield is supported by choking in the inlet throat. Here, the inlet throat is not choked during the unstart event, and advancement of the shock wave is supported by the constant-pressure exit boundary condition. In both cases however, as the terminal shock advances through the increasing Mach number of the compressive flowfield, the total pressure downstream decreases, thereby reducing the ability of either exit boundary condition to pass airflow. In the case of a choked area, this is easily understood since the airflow only depends on the total pressure. Imposing a constant static pressure at the exit however, causes an additional impediment to airflow as the local subsonic Mach number must also decrease. For constant total temperature, the mass flow through a given area is proportional to the product of total pressure and A*/A:

$$\dot{m} \propto P_t * \left(\frac{A^*}{A}\right)$$

For a choked area, where the area ratio function is unity, the sensitivity to total pressure is simply:

$$\frac{\partial \dot{m}}{\partial P_t} \propto 1$$

However, if static pressure is held constant as total pressure varies, the Mach number also varies, and the sensitivity becomes:

$$\frac{\partial \dot{m}}{\partial P_t} \propto P_t * \frac{\partial}{\partial P_t}\left(\frac{A^*}{A}\right) + \left(\frac{A^*}{A}\right)$$

These sensitivities are plotted in Figure 16 as a function of total-to-static pressure ratio, with the corresponding Mach number at the constant pressure boundary shown for reference. It is apparent that as total pressure decreases at the outflow boundary, the constant-pressure boundary requires a much larger reduction in mass flow than the choked area. For example, at the highest stable back-pressure in the present simulation, the ratio of total-to-static pressure is 1.17, and the sensitivity of mass flow to total pressure for the constant-pressure boundary is at least twice that of a choked area. That is to say, for an incremental reduction in total pressure at the advancing shock wave, the constant-pressure exit boundary condition will reduce the flow rate by twice that of a choked area.

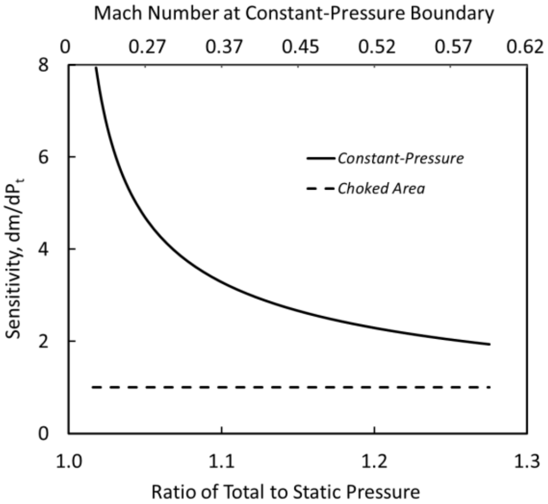

Fig. 16 Sensitivity of mass flow per unit area to changes in total pressure for constant-pressure, and choked outflow boundary conditions.

The second difficulty in using the constant-pressure exit boundary condition arises from the behavior of the static pressure at the AIP as airflow demand is reduced. Figure 17 shows the static pressure ratio at the AIP versus mass flow ratio for the Ref. [1] solutions that used a choked nozzle boundary condition, and the present case where the static pressure is imposed. The total pressure downstream of a freestream normal shock was chosen as the reference for this pressure ratio as it is related to the maximum pressure that could be developed at the AIP. The Ref. [1] case shows a maximum at slightly subcritical conditions, followed by a reduction in static pressure as the mass flow ratio is further reduced. Given this somewhat non-intuitive characteristic, it is obvious that the constant-pressure exit boundary condition cannot be used to map sub-critical operation of the present inlet configuration and flight condition, nor any other with a similar characteristic.

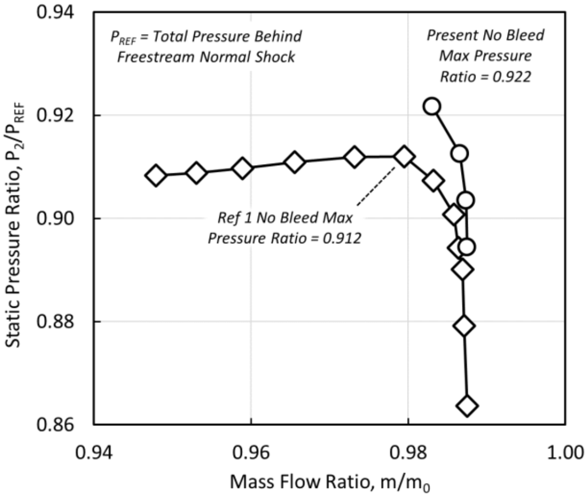

Fig. 17 Comparison of static pressure ratio at the AIP versus mass flow ratio between choked nozzle and constant-pressure exit boundary conditions.

VI. Summary and Conclusions

The Bay model in Wind-US was used successfully to model the effects of a co-rotating vortex generator array, resulting in significant computational savings. Results with no vortex generators compared well to the no-bleed cases of Ref. [1], with the exception of significantly reduced subcritical stability margin. The addition of vortex generators resulted in only slight improvements in recovery and distortion, and did not increase subcritical stability margin. These improvements were substantially less than those reported in Ref. [1] for boundary-layer bleed, although the comparison is complicated by the back-pressure limitation of the present simulations.

A time-accurate simulation was performed to better understand the unstart process that limited the subcritical range. A one-half percent increment in back-pressure initiated a steady upstream advance of the terminal shock to the cowl lip. This was followed by an unsteady fluctuation that transitioned to limit-cycle behavior at a frequency of 40Hz. Pressures on the internal inlet surfaces did not substantially exceed the imposed back-pressure. Two instantaneous solution images, taken during the forward advance of the terminal shock, compared almost identically to steady, subcritical solutions shown in Ref. [1].

Further investigation revealed that there is a maximum back-pressure at a slightly sub-critical mass flow ratio, followed by a reduction in back-pressure as mass flow ratio is further reduced. This characteristic renders the constant-pressure exit boundary condition useless for sub-critical simulation of the present inlet configuration and flight condition. No conclusion on the generality of this result can be drawn from the present work. It was also shown that the constant-pressure exit boundary condition is more restrictive to mass flow than a choked nozzle due to higher sensitivity to total pressure.

VII. References

[1] Otto, Samuel E., Trefny, Charles J., and Slater, John W., “Inward-Turning Streamline-Traced Inlet Design Method for Low-Boom, Low-Drag Applications,” AIAA Journal of Propulsion and Power, Vol. 32, No. 5, September 2016.
[2] Yoder, Dennis A., “Wind-US User’s Guide Version 4.0,” NASA/TM 2016-219145, September, 2016.
[3] Bender, E. E., Anderson, B. H., and Yagle, P. J., "Vortex Generator Modeling for Navier-Stokes Codes," FEDSSM99-69 19, 3rd Joint ASME/JSME Fluids Engineering Conference, San Francisco, California.
[4] Dudek, J. C., "Modeling Vortex Generators in a Navier-Stokes Code," AIAA Journal, Vol 49, No. 4, pp. 748-759
[5] Moore, M. T., “Distortion Data Analysis,” Air Force Aero Propulsion Laboratory contract 33615-72-C-1763 final report, AFAPL-TR-72-111, December, 1972.
[6] Steenken, W. G., Williams, J. G., Yuhas, A. J., and Walsh, K. R., “An Inlet Distortion Assessment During Aircraft Departures at High Angle of Attack for an F/A-18A Aircraft,” NASA TM-104328, 1997.